

A Nanoscale Investigation of Carlin-Type Gold Deposits: An Atom-Scale Elemental and Isotopic Perspective

Phillip Gopon,^{1,†} James O. Douglas,² Maria A. Auger,^{2,3} Lars Hansen,¹ Jon Wade,¹ Jean S. Cline,⁴
Laurence J. Robb,¹ and Michael P. Moody²

¹Department of Earth Science, University of Oxford, South Parks Rd., Oxford OX1 3AN, United Kingdom

²Department of Materials, University of Oxford, Parks Rd., Oxford OX1 3PH, United Kingdom

³Physics Department, Universidad Carlos III de Madrid, Avd. de la Universidad, 30.28911 Leganés (Madrid), Spain

⁴Department of Geoscience, University of Nevada Las Vegas, Las Vegas, Nevada 89154, USA

Abstract

Carlin-type gold deposits are one of the most important gold mineralization styles in the world. Despite their economic importance and the large volume of work that has been published, there remain crucial questions regarding their metallogenesis. Much of this uncertainty is due to the cryptic nature of the gold occurrence, with gold occurring as dispersed nanoscale inclusions within host pyrite rims that formed on earlier formed barren pyrite cores. The small size of the gold inclusions has made determining their nature within the host sulfides and the mechanisms by which they precipitated from the ore fluids particularly problematic.

This study combines high-resolution electron probe microanalysis (EPMA) with atom probe tomography (APT) to constrain whether the gold occurs as nanospheres or is dispersed within the Carlin pyrites. APT offers the unique capability of obtaining major, minor, trace, and isotopic chemical information at near-atomic spatial resolution. We use this capability to investigate the atomic-scale distribution of trace elements within Carlin-type pyrite rims, as well as the relative differences of sulfur isotopes within the rim and core of gold-hosting pyrite.

We show that gold within a sample from the Turquoise Ridge deposit (Nevada) occurs within arsenian pyrite overgrowth (rims) that formed on a pyrite core. Furthermore, this As-rich rim does not contain nanonuggets of gold and instead contains dispersed lattice-bound Au within the pyrite crystal structure. The spatial correlation of gold and arsenic within our samples is consistent with increased local arsenic concentrations that enhanced the ability of arsenian pyrite to host dispersed gold (Kusebauch et al., 2019). We hypothesize that point defects in the lattice induced by the addition of arsenic to the pyrite structure facilitate the dissemination of gold. The lack of gold nanospheres in our study is consistent with previous work showing that dispersed gold in arsenian pyrite can occur in concentrations up to ~1:200 (gold/arsenic). We also report a method for determining the sulfur isotope ratios from atom probe data sets of pyrite (\pm As) that illustrates a relative change between the pyrite core and its Au and arsenian pyrite rim. This spatial variation confirms that the observed pyrite core-rim structure is due to two-stage growth involving a sedimentary or magmatic-hydrothermal core and hydrothermal rim, as opposed to precipitation from an evolving hydrothermal fluid.

Introduction

The Carlin-type gold deposits in Nevada make up one of the largest gold districts in the world (Cline et al., 2005). These deposits contain an endowment of ~255 Moz (7,931 tonnes) of gold, of which 89% occurs in four main clusters of deposits, including the Carlin trend, Getchell, Cortez, and Jerritt Canyon (Muntean, 2018). The deposits occur along north-northwest to south-southeast trends in central Nevada and are characterized by cryptic gold mineralization in host carbonate rocks (Fig. 1). Gold within Carlin-type gold deposit tends to occur as ubiquitous trace element- and Au-rich pyrite rims that formed on unmineralized pyrite cores (Palenik et al., 2004; Barker et al., 2009).

The nature of the gold within the pyrite rims is important in determining the economic value of a deposit. Gold can either occur as dispersed lattice-bound Au⁺ throughout the host crystal structure or form spherical inclusions of Au⁰ within

the host grain. Because the gold is dispersed at the nanoscale, determining the structural location of the gold within the sulfide and the mechanisms by which it has been precipitated from its source hydrothermal fluids has been particularly problematic. The exact nature of the distribution of the gold within the host pyrite has substantial implications for the type of processing required to extract the gold (La Brooy et al., 1994) and leads to a new understanding of the Au precipitation mechanisms that made these deposits.

The processes that give rise to the presence of gold in pyrite have been widely debated. It has been known for some time (Wolthers et al., 2007; Barker et al., 2009; Deditius et al., 2014) that As and Au tend to be collocated within the pyrite, but the causal mechanisms for this correlation lacked direct evidence (Fleet and Mumin, 1997; Reich and Becker, 2006). Reich et al. (2005) suggested that the ratio of Au to As in the host sulfide reflects variable solubility as the fluid evolves and variable concentration ratios in the mineral's crystal structure (Deditius et al., 2014). Other authors have argued that it is the precipitation rate, rather than evolving As solubility, that plays

[†]Corresponding author: e-mail, phillip.gopon@earth.ox.ac.uk

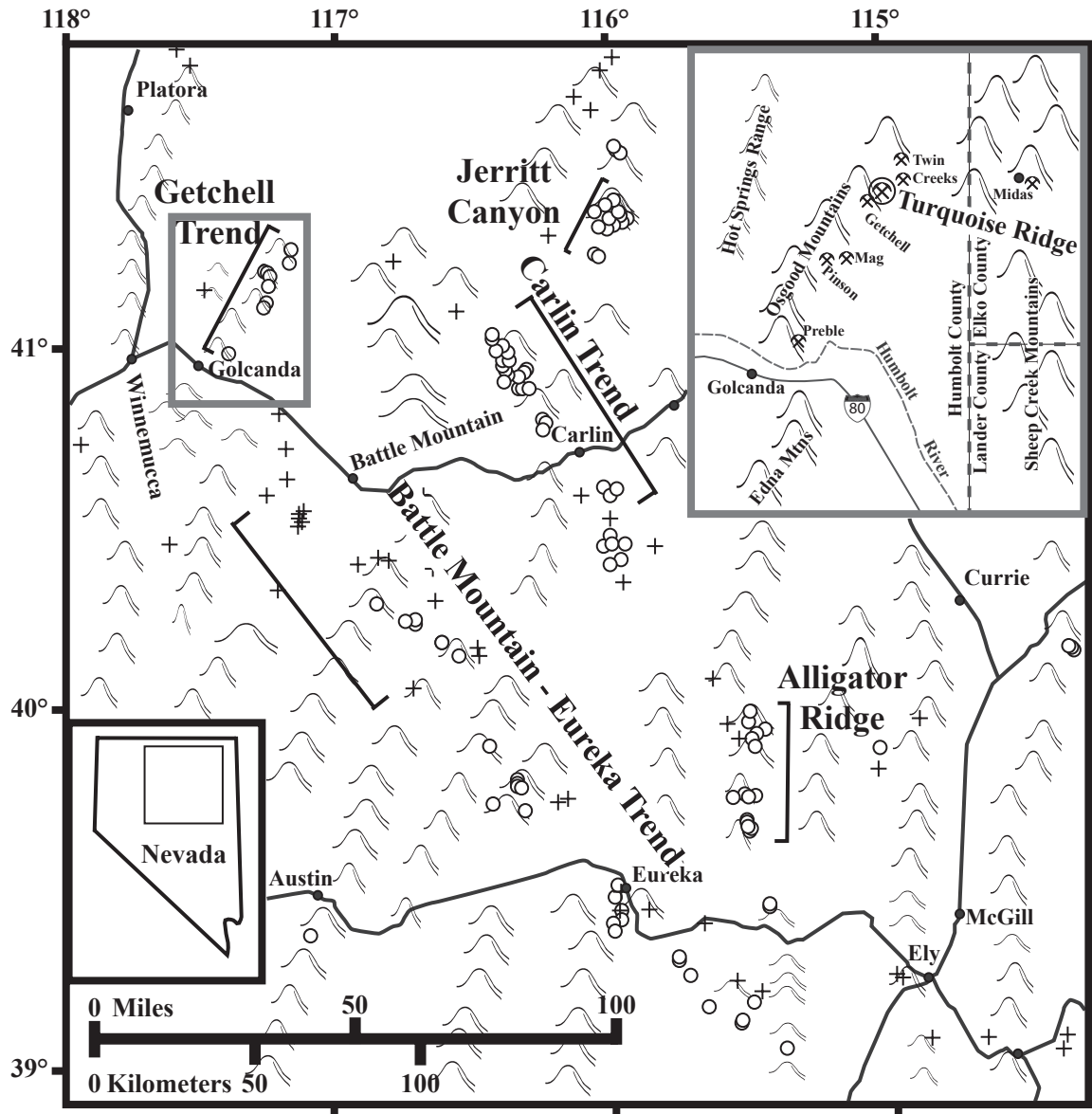


Fig. 1. Overview map of Carlin-type gold deposits in Nevada, showing the main Carlin-type gold deposit trends and the location of the Turquoise Ridge mine (shown in enlargement of boxed area in upper right). Inset map in lower left shows the location of figure area within Nevada. Modified from Cline et al. (2005).

a dominant role in the Au distribution within pyrite (Fougrouse et al., 2016).

Alternatively, Simon et al. (1999) determined that significant ionically bound Au^+ was present in ore pyrite at the Twin Creeks deposit. This indicated that abundant Au^+ could be adsorbed by arsenian pyrite from fluids that were not saturated in Au. They further concluded that as much as 50% of total Au in a deposit could be sourced from undersaturated fluids. Kusebauch et al. (2019), in an experimental study, determined that coupled partitioning of Au and As into pyrite produced high-grade ore and large Carlin-type Au deposits.

A complete understanding of the formation mechanisms of Carlin-type gold deposit, therefore, requires detailed knowledge of the spatial relationships between Au and concomitant trace elements. This detailed knowledge in turn requires

analytical techniques that possess both nanoscale spatial resolution and the elemental sensitivity required to confidently identify elemental correlations. To obtain elemental analyses at micrometer and nanometer scales, we use a combination of high-resolution electron probe microanalysis (EPMA) and atom probe tomography (APT). Combined, these techniques allow us to visualize the elemental distribution of gold and its associated elements at the required scale and hence elucidate the formation mechanism. High-resolution EPMA is used to acquire elemental data of both the surrounding silicate matrix and the hosting sulfide, with analytical volumes of ~ 300 nm (Gopon et al., 2013). Unlike many other micro-analytical techniques, EPMA offers high analytical spatial resolution and fully quantified elemental analyses of all major and minor elements with atomic mass greater than boron. In

contrast, APT offers major to trace element data, and potentially isotopic information in three dimensions. APT analytical volumes are generally ~ 80 nm in width and ~ 200 nm in depth, such that the absolute number of atoms measured is generally below ~ 100 million (Gault et al., 2012). However, analysis of the $<5\text{-}\mu\text{m}$ As/Au-rich pyrite rims in this study would have been difficult with laser ablation or secondary ion techniques. By combining these two complementary techniques, we can determine the chemistry of Carlin-type gold deposit at hitherto unexplored scales and, in doing so, better understand the controls on nanoparticle gold formation.

Geologic setting

Carlin-type gold deposits generally occur in a series of four main northeast or northwest trends of districts in north-central Nevada (Fig. 1). The deposits range in age from 42 to 34 Ma and coincide with the regional switch from a compressional to an extensional setting. Mineralization is structurally and stratigraphically controlled and disseminated in carbonate host rocks (Muntean et al., 2011). The Carlin-type districts in Nevada are thought to be associated with old reactivated basement rift structures (Cline et al., 2005). Carlin-type gold deposit have also been described in the Yukon Territory, Canada (Pinet et al., 2016) and in Guizhou, China (Su et al., 2009), although the China deposits appear to have formed at somewhat greater depth and higher temperature than the Nevada and Yukon deposits (Xie et al., 2018). The presence of only three identified areas of Carlin-type gold mineralization could be due either to the difficulty in finding disseminated gold deposits in general or to the rare conditions required to form these economically important gold deposits.

This study focuses on two representative Carlin-type gold deposit samples from the Turquoise Ridge and the Cortez Hills deposits in the Getchell and Battle Mountain trends, respectively. The Getchell trend deposits strike northeast to southwest in the Osgood Mountains of north-central Nevada (Longo et al., 2009). The Turquoise Ridge deposit is located in the northern portion of the Getchell trend ~ 50 miles northeast of Winnemucca and is proximal to an igneous intrusion and related W-Mo skarn deposits (Kirby and Riley deposits; Cline and Hofstra, 2000) formed at ~ 90 Ma. The sample is taken from a mudstone unit of the Ordovician Comus Formation, from the hanging wall of the Getchell fault (Longo et al., 2009). The Cortez Hills deposit, a large, cone-shaped collapse breccia, is located along the Battle Mountain-Eureka trend. The sample is from the lower part of the breccia deposit in the Devonian Roberts Mountains Formation (Maroun et al., 2017). These samples were chosen because they were deemed characteristic of the high-grade ore zones of these deposits. The APT component of this study focuses on the representative sample (TU664) from the Turquoise Ridge mine.

Methods

Samples for analysis in this study were selected from drill cores previously collected from the Turquoise Ridge and Cortez Hills deposits (northern Nevada). Drill core was originally collected on transects from low- or no-grade into high-grade ore to examine changes in host-rock mineralogy and ore and gangue formation related to gold deposition (Longo et al., 2009; Maroun et al., 2017). For this study, samples were

prepared for EPMA by mounting in 25-mm cold-cure epoxy rounds, sectioning, and polishing down to $1\text{-}\mu\text{m}$ grit size with an alumina suspension. Samples were then cleaned in a series of ethanol and distilled water sonic baths, dried, and vacuum evaporation coated with 20 nm of carbon.

The epoxy mounts were investigated using a number of different techniques. Scanning electron microscopy (SEM) and energy dispersive spectroscopy (EDS) using a FEI Quanta 650 FEG SEM was used to get an overall sense of the abundance and distribution of sulfides within the samples. A series of background-corrected X-ray maps were acquired on 10 randomly selected pyrite grains (five from Cortez Hills and five from Turquoise Ridge). These maps were acquired on a CAMECA SX5-FE EPMA (in the Department of Earth Science, University of Oxford) using a 25-keV and 200-nA electron beam. Because of the low abundance of gold in these samples, all five wavelength dispersive spectrometers (WDS) were calibrated on the Au peaks ($L\alpha$ at 25 keV and $M\alpha$ at 10 keV) and counts summed together. To improve the counting statistics further, a relatively long dwell time of 0.1 s per pixel was employed. One zoned grain from the Turquoise Ridge sample (TU664-G2) was selected for further higher-resolution mapping because of the stronger nature of the core/rim zoning as well as evidence of oscillatory zoning present within the rim. A further X-ray map was conducted at 10 keV (60 nA 0.2 s dwell time) for improved spatial resolution.

For APT sample preparation, we follow the preparation methods documented by Thompson et al. (2007). Three $2\text{-}\times\text{-}20\text{-}\mu\text{m}$ slices were taken from grain TU664-G2, using a Zeiss NVision FEG SEM equipped with focused ion beam (FIB) and a micromanipulator (Department of Materials, University of Oxford). Two of the lift-outs (APT samples R1 and R2) were targeted from the relatively Au rich rim of the grain to ensure the maximum number of APT specimens with enriched Au. The third lift-out (APT sample C1) was taken from the relatively Au poor core so a core-rim comparison could be made.

Because APT requires a highly sharpened ($<80\text{-nm}$ initial tip radius), needle-shaped sample to be subjected to a very high electric field while simultaneously exposed to a pulsed laser, specimens often fracture prior to the collection of a statistically useful number of ions. Because geologic materials are predominantly insulators, they are prone to fracturing in the high electric field of the APT (Gopon et al., 2017). To ensure that enough needle-shaped specimens were prepared to get at least one successful APT analysis each from the core and rim, 14 needle-shaped specimens (six from the core and eight from the rim) were prepared from FIB lift-outs parallel to the zoning.

APT analyses were conducted on a CAMECA LEAP 5000XR (in the Department of Materials, University of Oxford) in laser pulsing mode with a 355-nm laser. By iterating successive APT runs, we settled on a two-stage analytical routine to maximize analytical runtime and minimize sample tip failures. The analytical conditions were initiated at a specimen temperature of 50 K, 125-kHz laser pulse rate, 80-pJ laser energy, and 1% detection rate. In order to avoid wraparound and to ensure that the mass spectrum range exceeded 200 Dalton (Da) (Au^+ is at 197 Da), a combination of low pulse frequency and low laser energy was required for analysis. It was, however, challenging to align the laser to the sample using a low

laser pulse energy due to the reduced contribution of the laser to the evaporation process, which results in smaller changes in detection rate as a function of laser alignment. Therefore, a higher pulse laser energy of 80 pJ was used to align the laser to the sample, with the laser energy subsequently lowered to 40 pJ for the duration of the analysis.

Out of the 14 prepared APT specimens, three of the analyses were successful: two from the rim and one from the core. The successful analysis from the core region was stopped once a data set of 20 million ions was acquired, while in the two analyses from the rim the specimen fractured at 5 million and 4 million ions, respectively. The APT analyses from sample TU664-G2 will hereafter be referred to as rim analyses 1 and 2 (R1, R2) and core analysis 1 (C1).

Reconstructions of the APT data sets were conducted in the CAMECA IVAS software package (v 3.6). Protocols for mass to charge state ratio peak identification and ranging were based on Fougere et al. (2016). All peaks with a height greater than twice that of the background level were identified and ranged (App. Table A1). The resulting mass spectra from the core and the rim included peaks comprising polyatomic ions (for instance, S₂, S₃, AsS). To determine the validity of our APT mass spectra element selection, EPMA measurements of the sample's sulfides were used to justify these element choices (App. Fig. A1). Local elemental concentrations were then applied to the reconstructed data using the 3Depict software (Haley, 2018).

Sulfur isotope contents were also investigated with APT. Because of isobaric interferences on the main sulfur peaks (Ni⁺⁺ on S⁺ at 32 Da; Ge⁺⁺ on S⁺ at 36 Da; S₂⁺ on all S⁺ at 32, 33, 34, and 36 Da), these were determined from a combination of the S₂⁺ and AsS⁺ peaks. The rim contains enough As to give substantial AsS peaks, which have no mass to charge state ratio overlaps, to derive ³⁴S/³²S ratios. However, because the core contains only trace amounts of As, there are no significant AsS peaks to derive ³⁴S/³²S ratios. The relative isotopic difference between the core and rim can, however, be derived by utilizing the S₂⁺ peaks that exhibit no isobaric interferences. To achieve this, a spectral deconvolution algorithm was used to obtain the ³⁴S/³²S and ³³S/³²S ratios from the S₂⁺ mass spectra as follows.

First, the integrated area under each peak of interest is obtained from the APT data set. Peaks are analyzed at ³²S³²S 64, ³²S³³S 65, ³³S³³S, and ³²S³⁴S 66, ³³S³⁴S 67, and ³⁴S³⁴S 68 Da. The S₂ peak at 65 Da is corrected for a minor interference with Cu based on the natural abundance of Cu and the amount measured as the ⁶³Cu isotope using the equation

$$S_{65} \text{ cnts} = \text{total 65 cnts} - ([\text{total 63 cnts} \times 30.85]/69.15). \quad (1)$$

Second, an optimization routine was used to find the set of values for ³²S, ³³S, ³⁴S, ³⁶S that best reproduces the observed values for peaks at 64, 65, 66, 67, and 68 Da. This optimization routine is performed as a grid search, in which the values of ³²S, ³³S, ³⁴S, ³⁶S are systematically changed, and the corresponding values for 64, 65, 66, 67, and 68 Da are calculated for each combination of S isotopes. In calculating the values of 64, 65, 66, 67, and 68 Da, all combinations of S isotopes are considered equally probable (e.g., ³³S³³S is considered just as likely as ³²S³⁴S, and both contribute to 66 Da). We define the best-fit combination as the one that minimizes the sum of squared residuals between the observed values and measured values of 64, 65, 66, 67, and 68 Da (Fig. 2).

An internal check on the validity of the deconvolution at the S₂ peaks is provided by the data sets that contain As, which independently provide a ³⁴S/³²S ratio. A thorough check of the influence of changing the ranging of the S₂ peaks was undertaken and compared to the S isotope results from the AsS peaks. Once an area of the peak larger than full width three-quarters of the maximum was ranged, the S isotope ratios determined from our program only changed by 0.02%. Based on this assessment a fixed bin width larger than the peak width was used and applied to all data sets (62.84–63.09; 63.68–64.68; 64.74–65.14; 65.68–66.56; 66.76–67.11; 67.74–68.18).

A full determination of the uncertainty of our measurement requires incorporating the full instrumental uncertainty estimates into our deconvolution script, which is beyond the scope of the current work. We do note that our signal to noise ratio is greater than 10:1 (App. Fig. A1), which is the threshold at which previous work deemed the uncertainty from the

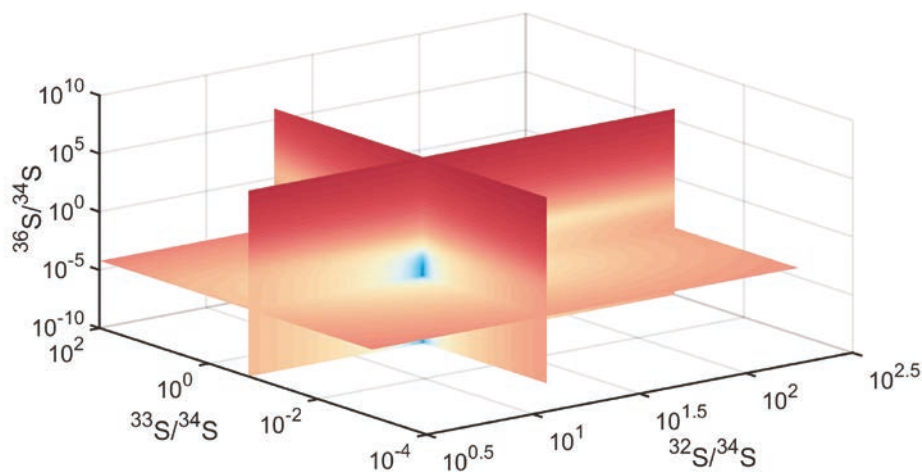


Fig. 2. 3-D plot of the misfit between the data and answer generated in the deconvolution script of the ³²S, ³³S, and ³⁶S peaks normalized to ³⁴S for data set R1. Colder colors (blue) correspond to lower misfit, and warmer colors (red) to a high misfit. The solution of the algorithm is the intersection of the three misfit planes.

peak to background measurement to be negligible (Daly et al., 2018). The uncertainty in our deconvolution algorithm is similarly low, with a 95% confidence interval of $\sim 0.3\%$ for the $^{34}\text{S}/^{32}\text{S}$ ratio. A further test of the uncertainty in our deconvolution was provided by the simulation of pyrite mass spectra using the MATLAB script presented in London (2019). We simulated a series of atom probe mass spectra with variable input S isotope ratios and assessed the simulated spectrum with the above-described S_2 deconvolution algorithm. Our deconvolution script is able to generate the starting $^{34}\text{S}/^{32}\text{S}$ ratio to within 0.8% for all simulated spectra. A further consideration is the uncertainty added by the deconvolution of the 65 peak, which is accomplished by assuming natural isotopic abundance for Cu. Removal of the Cu deconvolution step only modifies the calculated S isotope ratio by 3%, as any real

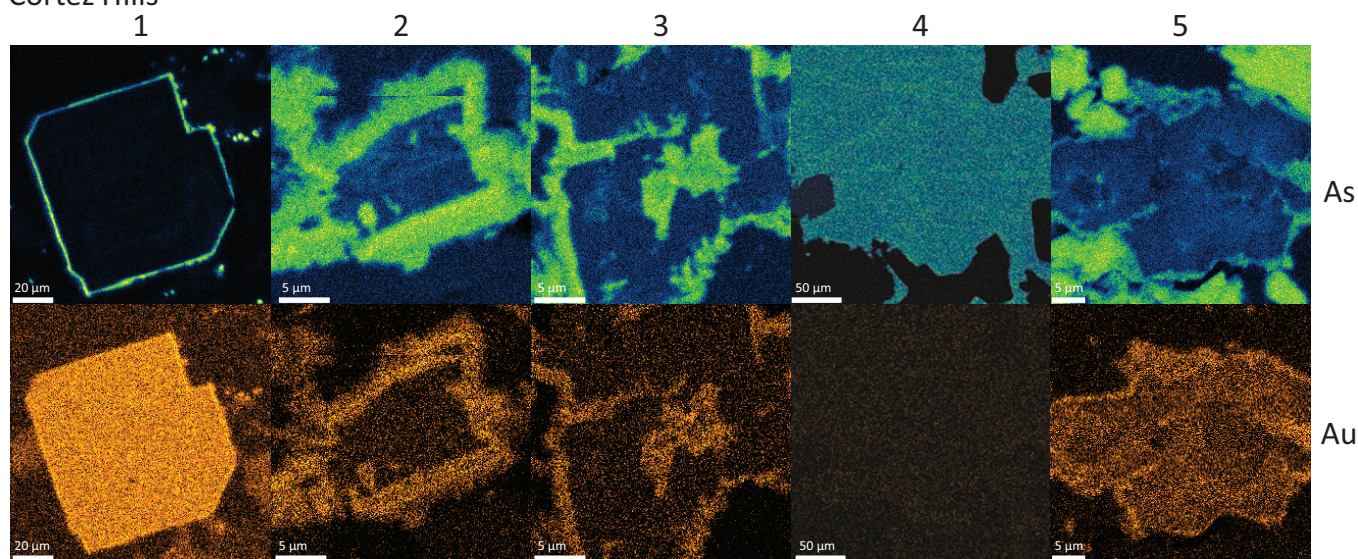
change in Cu isotopes will be small and will have a negligible effect on the resulting $^{34}\text{S}/^{32}\text{S}$ ratio.

Results

EPMA results

Figure 3 shows the results of a select number of X-ray maps (conducted at 25 keV) from the Turquoise Ridge (TU664) and Cortez Hills (CHUE-019) deposits. As evident in these images, there is a correlation between arsenic abundance and the presence of gold. All but two grains mapped show at least two distinctive regions (core and rim), with core being relatively devoid of gold and arsenic, while the rim is comparatively rich in arsenic and gold. All of the maps from the Turquoise Ridge sample showed some evidence of oscillatory zoning in the rim,

Cortez Hills



Turquoise Ridge

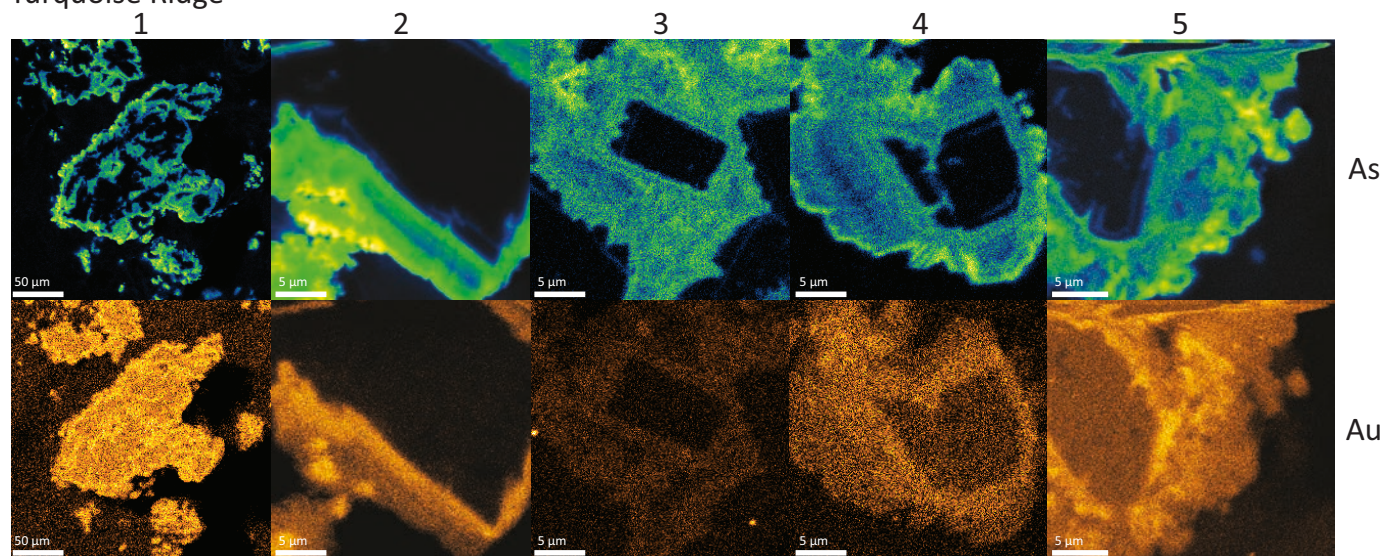


Fig. 3. EPMA X-ray maps for As showing the five grains from Cortez Hills (top) and Turquoise Ridge (bottom). Turquoise Ridge grain 2 was chosen for the following APT investigation.

while the Cortez Hills samples do not show evidence for oscillatory zoning in the rim, or the zoning is too fine to be seen by EPMA. Turquoise Ridge grains 2 and 4 showed the best examples of submicron-scale concentric oscillatory zoning.

Oscillatory zoning in arsenian pyrite, surrounding As/Au-poor core

The oscillatory zoning is of particular interest, as it suggests either pulsed fluid flow and/or variable physicochemical conditions of metal precipitation, presumably over a relatively abbreviated time span. In order to resolve which mechanism was dominant, a second set of higher-resolution maps was acquired (at 10 keV) for the same grains. Figure 4 shows the higher-resolution maps for grain TU664-G2, showing the submicron oscillatory zoning present in the rim. There appears to be at least nine distinct As zones in the rim of grain TU664-G2 compared to only two Au zones over the same rim interval (Fig. 4). It should be noted that at 10 keV the gold X-ray yield is low, and we may not have the signal required to see zoning. However, when comparing the 25-keV As and Au maps (where we have more signal) there does not seem to be a 1:1 correlation between As-rich areas and high Au. This does not seem to be the case when looking at the S versus As maps (Fig. 4), where a significant anticorrelation seems to be present. It also appears that the first few increments (labeled as 7, 8, and 9 on Fig. 4b, c) of arsenian pyrite crystal growth in the rim contained an appreciable amount of gold (~200 ppm from APT).

The core of the grain, while not as intricately zoned as the rim, does show at least three distinct zones. The interior is devoid of As and is surrounded by a region slightly enriched in As, with an outer As-absent region that borders the As-rich rim.

APT results

Three out of the 14 APT needle-shaped specimens that were prepared from TU664-G2 generated successful APT data sets (Fig. 5). Two of the smaller data sets (R1, R2) were obtained from the gold-rich rims, and the largest data set (C2) came from the core of the pyrite grain (Fig. 4). APT confirms that the core of pyrite grain TU664-G2 is devoid of gold as well as arsenic. The data sets R1 and R2 came from gold-rich bands directly adjacent to the core. The core of TU664-G2 is pure pyrite with no detectable arsenic, gold, potassium, or mercury. The rim of this grain contains ~200 ppm gold and >5 at. % arsenic (Fig. 5). The rim is also noteworthy, because it contains a notable suite of trace elements, including potassium (60 ppm; detected using the K⁺ peaks) and mercury (80 ppm; detected using the Hg⁺ peaks). The average maximum background level for the three data sets is ~40 counts; this translates to a detection limit of ~3 ppm.

The trace elemental signature of the rim is much more complex than the core (Fig. 4) and contains appreciable amounts of arsenic, gold, potassium, and mercury. However, in our sample there was no obvious atomic clustering and a nearest neighbour analysis (conducted with the IVAS software) found no statistical evidence for gold clustering in either the core or the rim of this particular grain. Previous studies have reported nanospheres of gold within arsenian pyrite (Palenik et al., 2004; Reich et al., 2005), so the absence of such Au nanospheres in our samples is noteworthy.

Figure 6 shows the distribution of relative local concentrations for a radius of 2.5 nm surrounding each individual gold ion in the APT reconstruction (blue). To enable interpretation, a complementary data set was generated by randomizing the spatial distribution of all elements in the original APT reconstructions, and the local concentration analysis was reapplied (red). The Y axis shows the number of Au ions that contain a given relative concentration of As. Relative concentration is defined as the ratio As/(Fe + As). The distribution for the real data is broader with more regions of higher concentrations compared to the randomized data set. These statistics indicate that there is a higher arsenic concentration surrounding each gold ion compared to the bulk (randomized data set).

The results of our S isotope study corroborate the differences in trace elements noted between the core and rim and show a 0.0057 shift (12.8%) in ³⁴S/³²S between the core (0.0503) and rim (0.0446) (Fig. 5).

Discussion

Major elemental zoning

Of particular note is the presence of weakly zoned core and markedly oscillatory zoned rims in terms of As and Au contents. This zonation reveals that the pyrite core and rim could have formed in at least two, and up to 12, discrete increments. Oscillatory zoning in pyrite has been noted by Wu et al. (2019) to be caused by diffusion-limited self-organization of a single continuous fluid pulse, and we cannot rule out this mechanism as the cause of our zoning.

The rim of the pyrite core is enriched in As and Au, as well as other fluid mobile trace elements (Fig. 5); the presence of K as a trace element reflects the possible presence of a saline fluid. The lack of As and Au in the core does not point as strongly to a fluid source—or at the very least not a sulfur- or gold-carrying fluid. This leaves us with a number of alternatives for the source of the Au/As-poor core of the grain; it could be interpreted as sedimentary, diagenetic, magmatic-hydrothermal, or hydrothermal. The sample TU664 was obtained from a laminated tuffaceous mudstone unit interbedded with limestones (Longo et al., 2009), suggesting the pyrite is sedimentary in origin and grew during diagenesis in reduced pockets of the mudstone. Although we favor a diagenetic origin for the pyrite cores, the presence of a region of increased As (zone 11, Fig. 4) is problematic, as sedimentary pyrite typically contains low trace element concentrations (Seal, 2006; Gregory et al., 2015). Magmatic-hydrothermal pyrite can show zoning if the fluid composition changes over time. It is possible that the increased As in zone 11 of the core is related to an earlier pulse of fluid migration, related to the same intrusion that formed the nearby 90 Ma W-Mo Kirby and Riley skarn deposits (Cline and Hofstra, 2000). Our current EPMA and APT data cannot further discriminate the source of the pyrite core, and the origin of this generation of pyrite in Carlin-type gold deposits remains enigmatic; however, the geologic evidence can place further constraints.

Evidence from trace elements

In comparison to the core, the rim is highly enriched in As, and the presence of Hg and K (which is often associated with saline hydrothermal fluids) indicates a hydrothermal origin

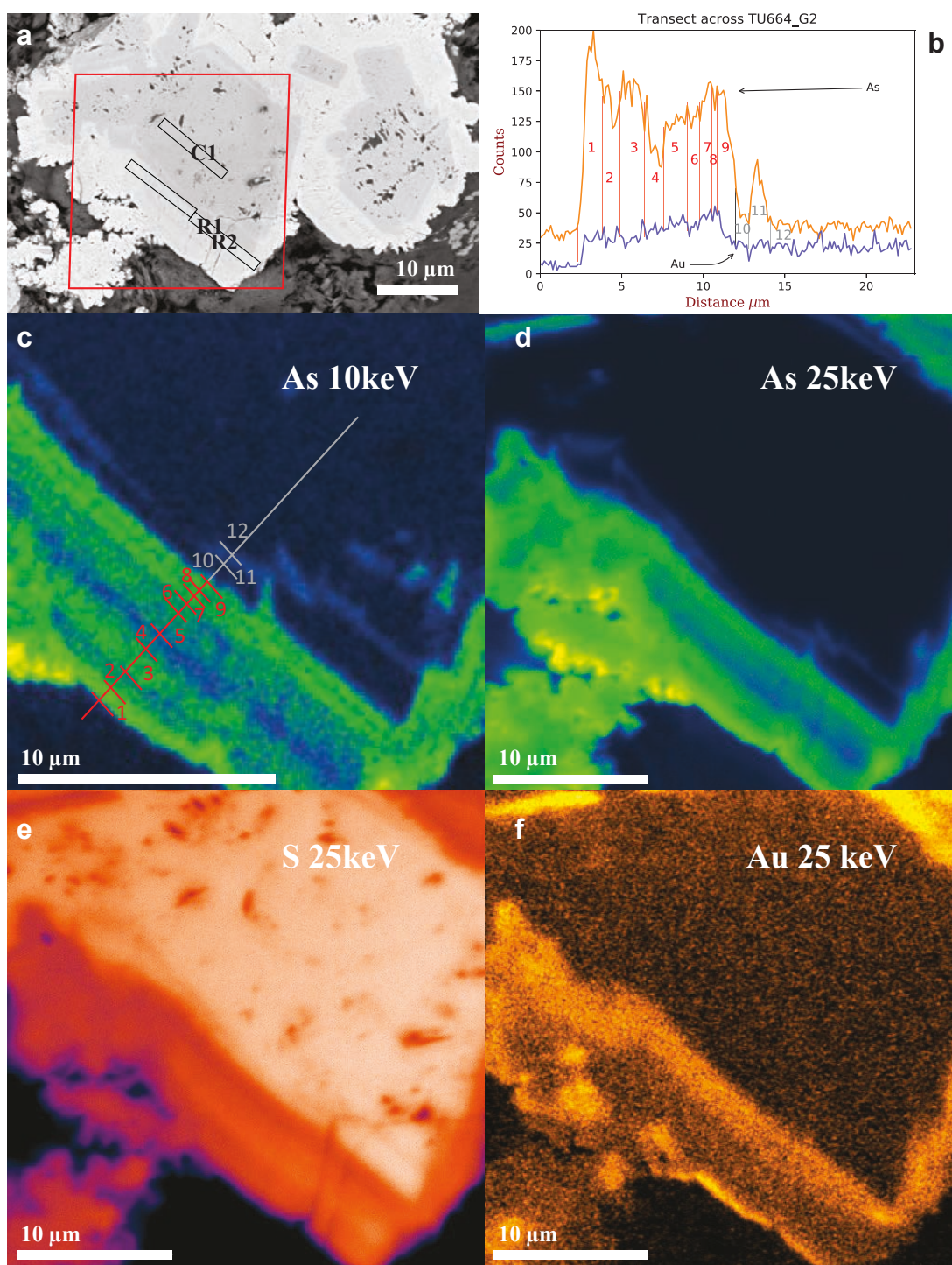


Fig. 4. Backscattered electron image (a), a linear As/Au profile (b), and EPMA X-ray intensity maps (c-f) from sample TU664 grain 2. Note the improvement in spatial resolution in the 10-keV versus 25-keV map. The 10-keV As map shows the transect line shown in (b) and outlines the approximately nine oscillatory zones in the As pyrite rim. Black bars on top left image are the regions that were lifted out by FIB-SEM and prepared for APT, and the approximate locations of APT samples C1, R1, and R2 are marked.

for the rim of the grain—an origin likely to have been different from that of the cores. At least nine chemically distinct submicron zones are present within the rim, suggesting relatively short-lived pulses of hydrothermal fluids rather than a single, long-lived one. The absence of fluid-mobile trace

elements, especially As, Au, Hg, and K, in the core as compared to their presence in the rim, either attests to significant changes in fluid composition between core and rim deposition or suggests that the core is magmatic-hydrothermal or sedimentary in origin and is not related to the ore-forming

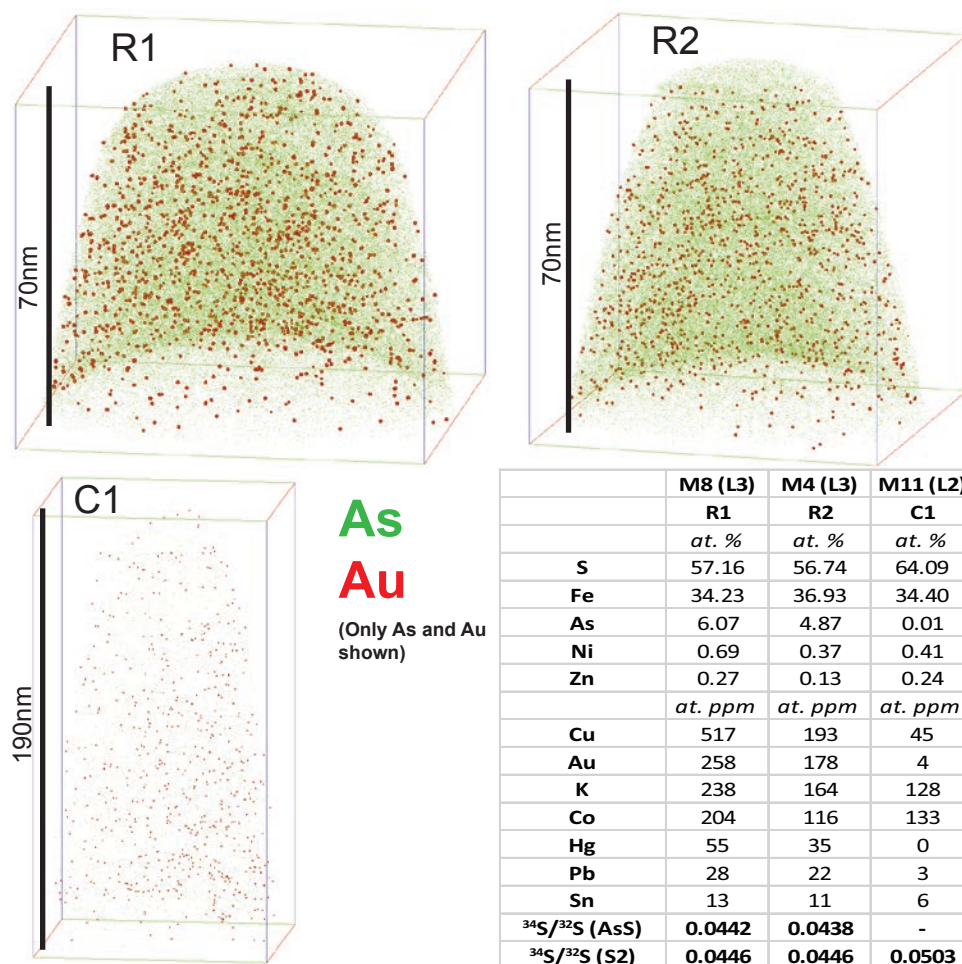


Fig. 5. APT reconstructions of R1, R2, and C1 showing only the As and Au ions. The table shows chemistry and $^{34}\text{S}/^{32}\text{S}$ ratios determined from the atom probe data sets, using the AsS peaks (labeled AsS) and the deconvolution algorithm on the S2 peaks (labeled S2).

process. Although the low levels of core-hosted trace elements do not allow us to positively identify the pyrite's formation mechanism, the order of abundance of trace metals in the core ($\text{Ni} > \text{Zn} > \text{Co} > \text{Cu} > \text{Sn} > \text{Au} > \text{Pb}$) does not match with sedimentary pyrite (Gregory et al., 2015). Field relationships might suggest a magmatic-hydrothermal source linked to nearby W-Mo skarn mineralization (Cline and Hofstra, 2000); however, both of these links are tenuous. For this reason, we examined S isotopes, which helps us further discriminate the source of the core of the pyrite.

Evidence from sulfur isotopes

The S isotopes derived from the APT data sets are limited due to the relatively low counting statistics inherent in APT, as well as the interferences on the main S peaks. Our deconvolution method for the S₂ peaks eliminates the interference issue. Our samples were not run against standards and therefore cannot be used to determine absolute $\delta^{34}\text{S}$ numbers. We acknowledge the absolute uncertainty of our measurements and seek only to present relative differences between the core and rim. Moreover, the AsS peaks present in the rim pyrite provide an independent method to measure the $^{34}\text{S}/^{32}\text{S}$ ratio (Fig. 5). This $^{34}\text{S}/^{32}\text{S}$ ratio measured at the AsS peaks is similar

to that measured at the S₂ peak, which validates our deconvolution algorithm and suggests that the 12.8% relative difference in $^{34}\text{S}/^{32}\text{S}$ between the core and the rim reflects different S sources for the different parts of the pyrite.

The $^{34}\text{S}/^{32}\text{S}$ ratios in the pyrite core are significantly heavier than the rim, which is inconsistent with formation by an evolving fluid. Moreover, this pattern of heavier core versus rim is the same as that found via nanoscale secondary ion mass spectrometry (nanoSIMS) by Barker et al. (2009) from similar samples from the Turquoise Ridge and Banshee Carlin-type gold deposit mines, supporting our isotopic findings. It should be reiterated that we are only reporting relative differences in $^{34}\text{S}/^{32}\text{S}$ between the core and rim. Further work is required before this relative difference in $^{34}\text{S}/^{32}\text{S}$ can be used to constrain whether the $\delta^{34}\text{S}$ of the core fits with a magmatic-hydrothermal or sedimentary pyrite source.

Implications of lack of gold nanospheres

The initial aim of this study was to investigate nanoscale gold clustering, so the lack of clustering within the arsenic-rich pyrite rim is noteworthy. We acknowledge that the lack of evidence for clusters does not necessarily prove its absence, but according to Palenik et al. (2004) we should have seen at

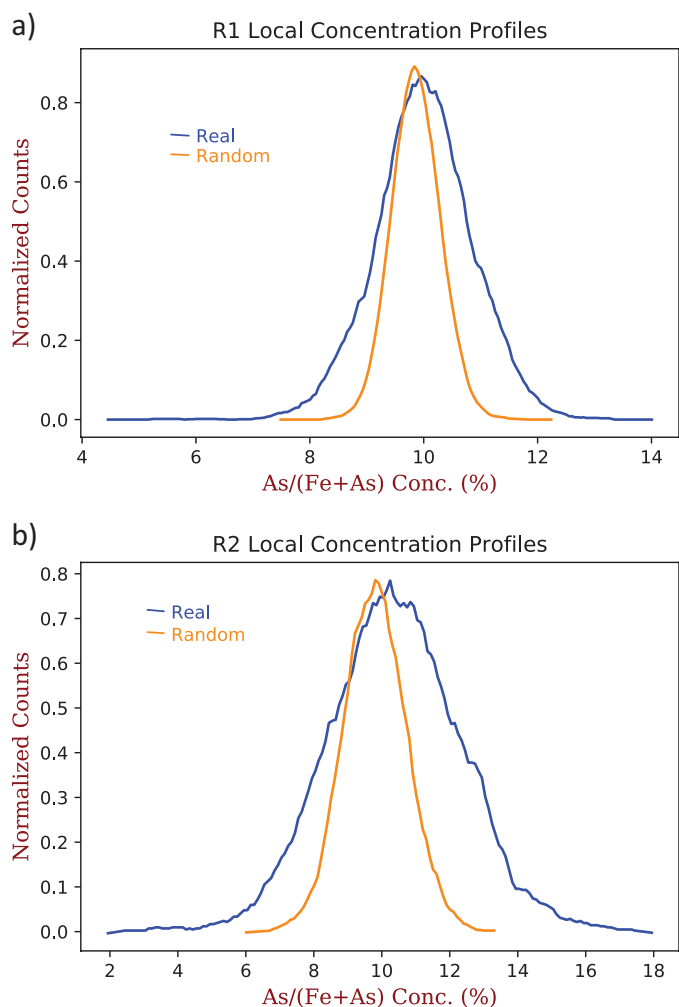


Fig. 6. Local concentration surrounding each Au ion, for data set R1 (a) and R2 (b). Y axis shows the number of Au ions that contain a given relative concentration of As. Relative concentrations given as concentrations As/(Fe + As).

least some gold nanoclusters within a ~50-nm area. We have sampled a region twice that large and have seen no evidence of gold nanoclusters. Our APT analyses of As content of pyrite rims is in keeping with the values reported by laser ablation-inductively coupled plasma-mass spectrometry by Large et al. (2011) and those in Appendix Table A1. Our gold values are, however, higher (10–170 ppm vs. our 178–268 ppm), which we attribute to the variability in the sulfide's gold content at the spatial resolution of the laser ablation technique used (>10 μm). The nanoscale resolution afforded by the APT technique allows the analysis of representative samples of both the host's core and the host's rim. This allows us to observe significant changes in the elemental concentration across these regions, which reflects the processes by which arsenian pyrite was formed and the gold concentrated within it.

The manner in which the gold occurs within arsenian pyrite is important for the recovery process of gold from these phases, and it is therefore important to understand why it occurs in different ways. Fougereuse et al. (2018) argue that the distribution of Au within arsenopyrite is controlled by the

rate of crystallization, i.e., the faster the crystallization rate the less likely nanoclusters are to form. Reich et al. (2005), on the other hand, suggest that a ratio of gold to arsenic within arsenian pyrite determines the point at which nanoclusters should start forming (Fig. 7). Arsenic-free systems also reduce Au^+ to Au^0 , so more Au^+ is available in an As-rich system to be incorporated in the lattice (Kusebauch et al., 2019). Since arsenian pyrite has a pyrite and not arsenopyrite crystal structure, the presence of arsenic will generate lattice defects. In this case, then, Au^+ is hosted as diffuse atoms within the small lattice defects. However, at the stage where the gold content of the crystal exceeds the 1:200 Au/As ratio, there is more Au^0 versus Au^+ available, and there are fewer lattice defects available to host gold, so gold will form Au^0 nanonuggets.

The Au/As ratios of the samples measured in this study (Fig. 7) are just below the threshold predicted by Reich et al. (2005) at which nanoclusters should begin to form. The combined chemical and 3-D information of the APT data set means that this is strong evidence that the Au/As ratio indeed controls the nanoscale distribution of gold in pyrite. Because we do not have an estimate of the growth rate of the Au-rich rim of the pyrite, we cannot totally dismiss the possibility that rapid growth rate (Fougereuse et al., 2016) was responsible for the lack of nanoclusters in the rim. However, the crystallographic differences between arsenopyrite (monoclinic) and arsenian pyrite (cubic) means that caution should be taken when drawing comparisons in their potential gold-hosting mechanisms.

Arsenic and gold colocalization

As shown in Figure 3, there is a relationship between gold and arsenic within the data sets that contain appreciable arsenic and gold. Where gold ions occur, there is an increased concentration of arsenic surrounding them (Fig. 6). This is of note, since it has previously been observed by Reich et al. (2005) and Deditius et al. (2014) that there seems to be a ratio of Au/As (~1:200; Fig. 7) below which gold is dispersed throughout the crystal structure and above which gold forms nanonuggets. Furthermore, Fleet and Mumin (1997) hypothesized that Au solid solution in pyrite could be accommodated by a combination of vacancies in nearest neighbor cation sites and fixed by soft Lewis bases (AsS , As_2). Our nanotextural evidence not only supports Reich's assertion that it is the ratio of Au/As that controls gold nanoparticle formation but also validates the mechanism hypothesized by Fleet and Mumin.

Arsenian pyrite's crystal structure is broadly that of pyrite (cubic) and not that of arsenopyrite (monoclinic). Arsenic in arsenian pyrite generally occurs as an anion (As^{1-}) and substitutes for S. It follows that the presence of arsenic replacing S results in the breaking of S-S bonds and will result in point defects and local charge within the crystal structure, which may accommodate Au (Fleet and Mumin, 1997). Thus, the more arsenic locally present, the greater the defect density surrounding the arsenic and, hence, the more gold that may be accommodated within these As-rich regions and dispersed throughout the arsenian pyrite crystal. While atom probe data does not give true crystallographic information, the data in Figure 6 combined with the findings of Reich et al. (2005) suggest that for roughly every 200 arsenic ions there can be

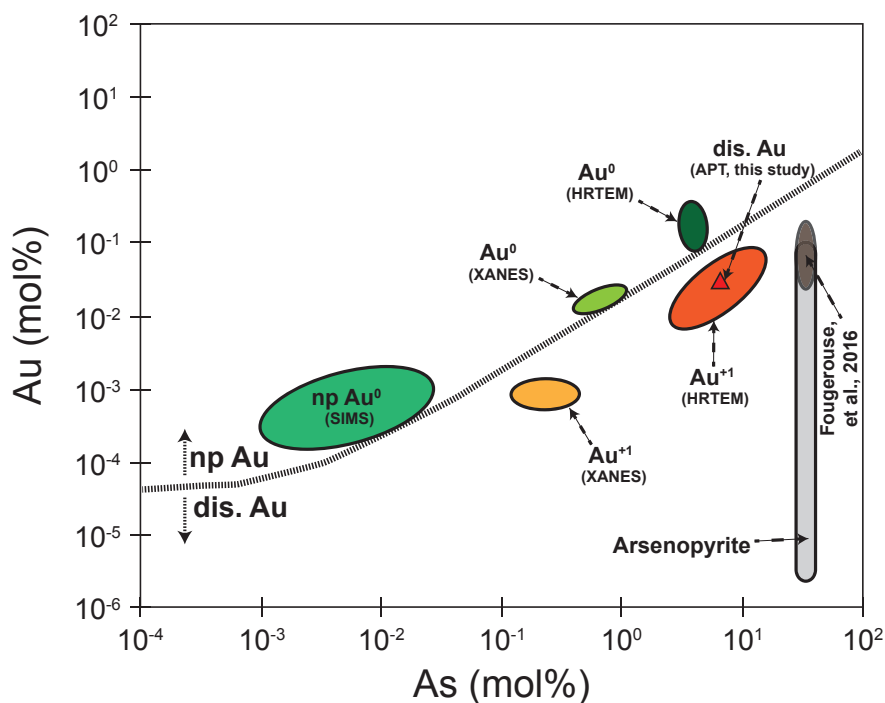


Fig. 7. Simplified As/Au ratio boundary graph; all fields taken from Reich et al. (2005). The hashed line represents the limit above which Au nanoparticles are meant to form. The Turquoise Ridge sample, labeled as “dis. Au (APT, this study),” sits slightly below the Au nanoparticle threshold, validating the position of the line. Abbreviations: dis. Au = dispersed gold, HRTEM = high-resolution transmission electron microscopy, np Au = gold nanoparticle, XANES = X-ray absorption near edge structure.

up to one gold ion accommodated within the defects generated. At yet higher local Au/As concentrations, however, the Au concentration is in excess of the available vacancy sites, such that the formation of Au nanoparticles becomes energetically favorable.

Conclusion

Although understanding the nanoscale nature of Carlin type gold mineralization has been fraught with difficulties, by visualizing the distribution of gold within pyrite at the micro- and nanoscales we can place additional constraints on the formation processes that led to this world-class gold district.

EPMA microanalysis reveals that, at the Turquoise Ridge deposit, the gold was deposited and formed from either nine discreet pulses of arsenic-rich fluids or a single pulse of an evolving As-rich fluid. The initial pyrite cores, which acted as substrates for the arsenian pyrite gold host, were sourced from a barren fluid related to either sedimentary or magmatic-hydrothermal processes. Trace elements from EPMA and APT suggest that this arsenic-rich, gold-bearing fluid was saline and contained appreciable amounts of potassium.

APT shows that gold is absent in the core of the pyrite and in this deposit does not form nanoclusters of gold in the rim but is dispersed, with a local atomic Au/As ratio at or below 1:200. This supports the argument of Reich et al. (2005) that an important control on the distribution of gold within arsenian pyrite is the ratio of Au/As (Fig. 7). Furthermore, our Au/As colocalization data (Fig. 6) suggest that the defects generated by the arsenic within the pyrite crystal structure are likely the reason a given amount of gold can be accommodated

within the crystal without the need to form nanoparticles. We do not have an estimate of pyrite growth rate so cannot dismiss growth rate (Fougerouse et al., 2016) as a control on Au distribution.

Sulfur isotopes and trace elements are both significantly different in the core and the rim, with the $^{34}\text{S}/^{32}\text{S}$ ratios in the core of the pyrite 12.8% heavier than the rim. Although further work is required to better constrain the relative $^{34}\text{S}/^{32}\text{S}$ and to determine the $\delta^{34}\text{S}$ of the gold-bearing rims to see if they have a magmatic or sedimentary signature, the presence of trace element enrichments, sulfur isotope compositions, and field-based relationships suggests hydrothermal deposition of arsenian pyrite around existing sedimentary or hydrothermal-magmatic pyrite cores.

Acknowledgments

We would like to acknowledge Andrew London for his help with simulating APT mass spectra to test our S_2 deconvolution algorithm, Barrick Gold Corporation for access to the samples and permission to publish these findings, and the entire Oxford Atom Probe Group for support with sample preparation and APT data reconstruction. Funding from the United Kingdom Engineering and Physical Sciences Research Council (EPSRC) under grants EP/K029770/1 and EP/M022803/1, as well as from the United Kingdom Environmental Research Council (NERC) under grant NE/K009540/1, is gratefully acknowledged. This manuscript benefited from careful reviews by Denis Fougerouse and Dan Gregory. All authors contributed equally to the writing of the manuscript.

REFERENCES

- Barker, S.L.L., Hickey, K.A., Cline, J.S., Dipple, G.M., Kilburn, M.R., Vaughan, J.R., and Longo, A.A., 2009, Uncloning invisible gold: Use of NanoSIMS to evaluate gold, trace elements, and sulfur isotopes in pyrite from Carlin-type gold deposits: *Economic Geology*, v. 104, p. 897–904.
- Cline, J.S., and Hofstra, A., 2000, Ore-fluid evolution at the Getchell Carlin-type gold deposit, Nevada, USA: *European Journal of Mineralogy*, v. 12, p. 195–212.
- Cline, J.S., Hofstra, A.H., Muntean, J.L., Tosdal, R.M., and Hickey, K.A., 2005, Carlin-type gold deposits in Nevada: Critical geologic characteristics and viable models: *Economic Geology 100th Anniversary Volume*, p. 451–484.
- Daly, L., Bland, P.A., Tessalina, S., Saxey, D.W., Reddy, S.M., Fougereuse, D., Rickard, W.D.A., Forman, L.V., La Fontaine, A., Cairney, J.M., Ringer, S.P., Schaefer, B.F., and Schwander, D., 2018, Defining the potential of nanoscale Re-Os isotope systematics using atom probe microscopy: *Geostandards and Geoanalytical Research*, v. 42, p. 279–299.
- Deditius, A.P., Reich, M., Kesler, S.E., Utsunomiya, S., Chryssoulis, S.L., Walshe, J., and Ewing, R.C., 2014, The coupled geochemistry of Au and As in pyrite from hydrothermal ore deposits: *Geochimica et Cosmochimica Acta*, v. 140, p. 644–670.
- Fleet, M.E., and Mumin, A.H., 1997, Gold-bearing arsenian pyrite and marcasite and arsenopyrite from Carlin trend gold deposits and laboratory synthesis: *American Mineralogist*, v. 82, p. 182–193.
- Fougereuse, D., Reddy, S.M., Saxey, D.W., Rickard, W.D.A., van Riessen, A., and Micklethwaite, S., 2016, Nanoscale gold clusters in arsenopyrite controlled by growth rate not concentration: Evidence from atom probe microscopy: *American Mineralogist*, v. 101, p. 1916–1919.
- Fougereuse, D., Reddy, S.M., Saxey, D.W., Erickson, T.M., Kirkland, C.L., Rickard, W.D.A., Seydoux-Guillaume, A.-M., Clark, C., and Buick, I.S., 2018, Nanoscale distribution of Pb in monazite revealed by atom probe microscopy: *Chemical Geology*, v. 479, p. 251–258.
- Gault, B., Moody, M.P., Cairney, J.M., and Ringer, S.P., 2012, Atom probe microscopy: Springer Series in Materials Science, v. 160, 411 p.
- Gopon, P., Fournelle, J., Sobol, P.E., and Llovet, X., 2013, Low-voltage electron-probe microanalysis of Fe-Si compounds using soft X-rays: *Microscopy and Microanalysis*, v. 19, p. 1698–1708.
- Gopon, P., Spicuzza, M.J., Kelly, T.F., Reinhard, D., Prosa, T.J., and Fournelle, J., 2017, Ultra-reduced phases in Apollo 16 regolith: Combined field emission electron probe microanalysis and atom probe tomography of sub-micron Fe-Si grains in Apollo 16 sample 61500: *Meteoritics and Planetary Science*, v. 22, p. 1–22.
- Gregory, D.D., Large, R.R., Halpin, J.A., Baturina, E.L., Lyons, T.W., Wu, S., Danyushevsky, L., Sack, P.J., Chappaz, A., Maslennikov, V.V. and Bull, S.W., 2015, Trace element content of sedimentary pyrite in black shales: *Economic Geology*, v. 110, p. 1389–1410.
- Haley, D., 2018, 3Depict: Valued point cloud visualisation and analysis software: <http://threedepict.sourceforge.net/>.
- Kusebauch, C., Gleeson, S.A., and Oelze, M., 2019, Coupled partitioning of Au and As into pyrite controls formation of giant Au deposits: *Science Advances*, v. 5, p. 1–8.
- La Brooy, S.R., Linge, H.G., and Walker, G.S., 1994, Review of gold extraction from ores: *Minerals Engineering*, v. 7, p. 1213–1241.
- Large, R.R., Bull, S.W., and Maslennikov, V.V., 2011, A carbonaceous sedimentary source-rock model for Carlin-type and orogenic gold deposits: *Economic Geology*, v. 106, p. 331–358.
- London, A.J., 2019, Quantifying uncertainty from mass-peak overlaps in atom probe microscopy: *Microscopy and Microanalysis*, v. 25, p. 378–388.
- Longo, A., Cline, J., and Muntean, J., 2009, Using pyrite to track evolving fluid pathways and chemistry in Carlin-type deposits, in Ressel, M.W., ed., *Diverse gold deposits of the Osgood Mountains and Humboldt Range, north-central Nevada*: Geological Society of Nevada, Special Publication 49, p. 63–65.
- Maroun, L.R.C., Cline, J.S., Simon, A., Anderson, P., and Muntean, J., 2017, High-grade gold deposition and collapse breccia formation, Cortez Hills Carlin-type gold deposit, Nevada, USA: *Economic Geology*, v. 112, p. 707–740.
- Muntean, J.L., 2018, The Carlin gold system: Applications to exploration in Nevada and beyond: *Reviews in Economic Geology*, v. 20, p. 39–88.
- Muntean, J.L., Cline, J.S., Simon, A.C., and Longo, A.A., 2011, Magmatic-hydrothermal origin of Nevada's Carlin-type gold deposits: *Nature Geoscience*, v. 4, p. 122–127.
- Palenik, C.S., Utsunomiya, S., Reich, M., Kesler, S.E., Wang, L., and Ewing, R.C., 2004, "Invisible" gold revealed: Direct imaging of gold nanoparticles in a Carlin-type deposit: *American Mineralogist*, v. 89, p. 1359–1366.
- Pinet, N., Mercier-Langevin, P., Dubé, B., Colpron, M., Lane, J., and Asselin, E., 2016, Lithotectonic controls on the genesis and distribution of carbonate replacement-type ("Carlin-type") gold zones, east-central Yukon: Targeted Geoscience Initiative, Geological Survey of Canada, v. 8199, p. 43–45.
- Reich, M., and Becker, U., 2006, First-principles calculations of the thermodynamic mixing properties of arsenic incorporation into pyrite and marcasite: *Chemical Geology*, v. 225, p. 278–290.
- Reich, M., Kesler, S.E., Utsunomiya, S., Palenik, C.S., Chryssoulis, S.L., and Ewing, R.C., 2005, Solubility of gold in arsenian pyrite: *Geochimica et Cosmochimica Acta*, v. 69, p. 2781–2796.
- Seal, R.R., 2006, Sulfur isotope geochemistry of sulfide minerals: *Reviews in Mineralogy and Geochemistry*, v. 61, p. 633–677.
- Simon, G., Kesler, S.E., and Chryssoulis, S., 1999, Geochemistry and textures of gold-bearing arsenian pyrite, Twin Creeks, Nevada: Implications for deposition of gold in Carlin-type deposits: *Economic Geology*, v. 94, p. 405–421.
- Su, W., Heinrich, C.A., Pettke, T., Zhang, X., Hu, R., and Xia, B., 2009, Sediment-hosted gold deposits in Guizhou, China: Products of wall-rock sulfidation by deep crustal fluids: *Economic Geology*, v. 104, p. 73–93.
- Thompson, K., Lawrence, D., Larson, D.J., Olson, J.D., Kelly, T.F., and Gorman, B., 2007, In situ site-specific specimen preparation for atom probe tomography: *Ultramicroscopy*, v. 107, p. 131–139.
- Wolthers, M., Butler, I.B., and Rickard, D., 2007, Influence of arsenic on iron sulfide transformations: *Chemical Geology*, v. 236, p. 217–227.
- Wu, Y.-F., Fougereuse, D., Evans, K., Reddy, S.M., Saxey, D.W., Guagliardo, P., and Li, J.-W., 2019, Gold, arsenic, and copper zoning in pyrite: A record of fluid chemistry and growth kinetics: *Geology*, v. 47, p. 1–4.
- Xie, Z., Xia, Y., Cline, J.S., Koenig, A., Wei, D., Tan, Q., and Wang, Z., 2018, Are there Carlin-type gold deposits in China? A comparison of the Guizhou, China, deposits with Nevada, USA, deposits: *Reviews in Economic Geology*, v. 20, p. 187–233.



Phillip Gopon is a postdoctoral researcher at the University of Oxford, United Kingdom. He received his Ph.D. degree (in petrology with Prof. John Valley and Dr. John Fournelle) and Master's degree (in economic geology with Prof. Phil Brown) from the University of Wisconsin-Madison, United States. Phil got his start in gold research during his master's studies, working with Newmont Mining to characterize the Sandman epithermal gold deposits in north-central Nevada. In addition to studying Carlin-type deposits at the nanoscale, he is also currently working with Prof. Laurence Robb (University of Oxford) to characterize gold mineralization in the Reguibat Shield of the Liberated Territories of Western Sahara.

